Microstructure-Controlled Ni-Rich Cathode Material by Microscale Compositional Partition for Next-Generation Electric Vehicles

Un-Hyuck Kim, Hoon-Hee Ryu, Jae-Hyung Kim, Robert Mücke, Payam Kaghazchi, Chong S. Yoon,* and Yang-Kook Sun*

A multi-compositional particulate $Li[Ni_{0.9}Co_{0.05}Mn_{0.05}]O_2$ cathode in which $Li[Ni_{0.94}Co_{0.038}Mn_{0.022}]O_2$ at the particle center is encapsulated by a 1.5-μm-thick concentration gradient (CG) shell with the outermost surface composition $Li[Ni_{0.841}Co_{0.077}Mn_{0.082}]O_2$ is synthesized using a differential coprecipitation process. The microscale compositional partitioning at the particle level combined with the radial texturing of the refined primary particles in the CG shell layer protracts the detrimental H2 → H3 phase transition, giving rise to sharp changes in the unit cell dimensions. This protraction, confirmed by *in-situ* X-ray diffraction and transmission electron microscopy, allows effective dissipation of the internal strain generated upon the H2 → H3 phase transition, markedly improving cycling performance and thermochemical stability as compared to those of the conventional single-composition $Li[Ni_{0.9}Co_{0.05}Mn_{0.05}]O_2$ cathode. The compositionally partitioned cathode delivers a discharge capacity of 229 mAh g^{-1} and exhibits capacity retentions of 88% after 1,000 cycles in a pouch-type full cell (cf. 68% for the conventional cathode). Thus, the proposed cathode material provides an opportunity for the rational design and development of a wide range of multi-functional cathodes, especially for Ni-rich NCM cathodes, by compositionally partitioning the cathode particles and thus optimizing the microstructural response to the internal strain produced in the deeply charged state.

Intro

Li-ion batteries (LIBs) have emerged as the main portable energy source for electric vehicles (EVs) owing to their high energy densities, high voltages, and long cycle lives as compared to those of other forms of secondary battery. One of the reasons for the success is that the energy density of LIBs at the cell level has increased two- to three-fold (gravimetric energy density from of 98 to 300 Wh kg^{-1} and volumetric energy density from 220 to 700 Wh L^{-1}) since LIBs were first introduced by Sony in 1991. However, currently available state-of-the-art LIBs are still inadequate for EVs that will appeal to a wider consumer base, mainly because of the short drive range per charge, which is limited by poor energy density, and their high costs when stacked against competing for fossil-fuel-powered internal combustion engine vehicles. The overall performance and cost of LIBs are largely determined by the cathode material because of its relatively low capacity and poor cycling stability compared to those of graphite, the most commonly used anode material, which can provide the high specific capacity of 372 mAh g^{-1} at a low material cost.[1]

Among the available cathode materials for LIBs, layered $LiMO_2$ (M = Ni, Co, Mn, or Al) is the material of choice owing to its high theoretical capacity of 275 mAh g^{-1}.[2-12] Over the last two decades, the Ni contents of $Li[Ni_xCo_yMn_z]O_2$ (NCM) or $Li[Ni_xCo_yAl_z]O_2$ (NCA) cathodes have gradually increased up to more than 90 mol%, providing reversible capacities of 227 mAh g^{-1} for $Li[Ni_{0.9}Co_{0.05}Mn_{0.05}]O_2$, 238 mAh g^{-1} for $Li[Ni_{0.95}Co_{0.025}Mn_{0.025}]O_2$, and 247 mAh g^{-1} for $LiNiO_2$, edging ever-closer to their theoretical capacities.[13-15] Ni-enriched layered cathodes, however, typically suffer from capacity fading and thermal runaway problems that become increasingly severe with increasing Ni content.[10,12,14,16,17] Capacity fading of Ni-rich layered cathodes, especially above $x = 0.8$, largely originates from the anisotropic volume change brought by phase transition (H2 → H3) near charge end (≈4.2 V).[14,15,18-20] This non-uniform lattice contraction and expansion during the phase transition generate internal microcracks that propagate to the particle surface, creating microchannels for electrolyte infiltration into the particle interior. Thus, the anisotropic volume change resulting from the phase transition not only destabilizes the mechanical integrity of the cathode particles but also further accelerates capacity fading by exposing the particle interiors to deleterious electrolyte attack.[14,15]

Among myriad strategies to overcome the inherent cycling instability of Ni-enriched cathodes, surface and grain boundary modification of the cathodes, in particular, based on atomic layer deposition (ALD) has been successful in alleviating the electrolyte attack of the internal surfaces.[21-22] ALD is superior in producing a thin uniform coating layer, but the process is capital intensive and the coating material is limited by the availability of precursors. Alternatively, we followed a more generic approach and developed a concentration gradient (CG) approach which is generally applicable to all kinds of cathode materials. We fabricated and tested a CG NCM cathode material that comprises particles, each of which has a Ni-enriched core and an outer layer that becomes progressively depleted of Ni and rich in Mn. High discharge capacity is provided by the Ni-enriched core while outstanding safety and stable cycling are gained from the Mn-rich outer layer, which protects the particle surface from parasitic reactions with the liquid electrolyte.[23-27] The CG approach is the most practical strategy for bringing the Ni-enriched NCM or NCA cathodes up to commercial standards reported so far. However, although the CG approach shows promise for providing energy densities that have the potential to deliver a driving range of more than 300 miles per charge, it is increasingly difficult to implement the scheme as the Ni content required is well above $x = 0.8$. The core, which is extremely rich in Ni, necessitates a prohibitively steep concentration gradient to accommodate the Ni-deficient surface.[27]

Accordingly, in this study, instead of continuous CGs comprising transition metal ions, we have revisited the core-shell structure that we proposed previously to develop a multi-compositional NCM cathode material in which $LiNiO_2$ is placed at the particle core and encapsulated by the well-tested Ni-rich NCM cathode material $Li[Ni_{0.8}Co_{0.1}Mn_{0.1}]O_2$.[23,27] After lithiation, the final composition of the core is $Li[Ni_{0.94}Co_{0.038}Mn_{0.022}]O_2$, providing a high capacity, while this core is surrounded by a 1.5-μm-thick CG shell with an outermost surface composition of $Li[Ni_{0.841}Co_{0.077}Mn_{0.082}]O_2$ (hereafter denoted as CSG90), as illustrated in **Figure 1**. The compositional partitioning at the micrometer level is designed to partially dissipate the internal strain accumulated by the detrimental H2 → H3 phase transition because the onset potential and the extent of the phase transition is highly dependent on the Ni content.[12,14,15] While the Ni-core is subjected to the abrupt lattice contraction from the formation of the H3 phase in the deeply charged state, the CG shell layer, whose phase transition is delayed because of its relatively low Ni content, can suppress microcrack nucleation in the particle core. In order to benchmark the effectiveness of the micrometer-scale compositional partitioning of the CSG90 cathode against a conventional single-composition cathode, the structural stability and electrochemical properties of the CSG90 cathode were intensively studied and compared with those of a conventional cathode with a similar average chemical composition (hereafter denoted as CC90).

Results and discussion

The average chemical compositions of the CC90 and CSG90 cathodes were both $Li[Ni_{0.9}Co_{0.05}Mn_{0.05}]O_2$, as determined by inductively coupled plasma mass spectrometry. As shown in Figure S1, the average particle size of the CC90 and CSG90 cathode materials is 11 μm in diameter, and both exhibit a narrow particle size distribution. X-ray diffraction (XRD) of the CC90 and CSG90 cathodes revealed that both have typical layered structures ($R\bar{3}m$) with little difference in lattice parameters

(Figure S2 and Table S1) as the lattice parameters for the CSG90 cathode closely match the average value of the constituent compositions. The concentration gradients of Ni, Co, and Mn within a CSG90 particle were quantitatively investigated using electron-probe X-ray microanalysis (EPMA). From the particle center up to 4 μm toward the particle surface, the composition remains nearly constant at $Li[Ni_{0.94}Co_{0.038}Mn_{0.022}]O_2$, and after this point the Ni concentration gradually decreases while both the Co and Mn concentrations increase smoothly, resulting in the particle surface composition $Li[Ni_{0.841}Co_{0.077}Mn_{0.082}]O_2$ (Figure S3a). On the other hand, the composition of the CC90 cathode material are uniform through the particle (Figure S3b).

The fundamental cell performances of the CC90 and CSG90 cathodes were characterized using a 2032 coin-type half-cell with Li metal as the anode and also a pouch-type full cell with graphite as the anode. As shown in **Figure 2a**, the CSG90 and CC90 cathodes deliver the same discharge capacity (228.7 mAh g^{-1}). The CC90 cathode, however, exhibits a rapid decrease in reversible capacity upon cycling, with a capacity retention of 85.2% after 100 cycles, which is typical of highly Ni-enriched NCM cathodes (Figure 2b). The capacity fading is presumably due to surface degradation, both in terms of the secondary particle surfaces and interparticle boundaries in the material bulk, caused by direct contact of reactive Ni^{4+} ions with the liquid electrolyte in the highly charged state.[14,15,28-30] As expected, the Li^+ intercalation stability of the CSG90 cathode is greatly improved as compared to that of CC90, showing a capacity retention of 92.2% for the same cycling period. The difference in the performance is further intensified in a high temperature test (60 °C); both cathodes show similar discharge capacity (~230 mAh g^{-1}) but the CSG90 cathode maintains 92% of its initial capacity after 100 cycles whereas the CC90 cathode retains only 81% (Figure S4). These are due to the high structural and chemical stabilities provided by the Mn-rich surface layer and the compositional partitioning.

To verify the improved structural stability of the CSG90 cathode, dQ dV^{-1} profiles were obtained by differentiating the charge and discharge curves (Figure 2c and 2d). Both cathodes show four distinct redox peaks arising from the multiple phase transitions in $Li_{1-x}[Ni_{0.90}Co_{0.05}Mn_{0.05}]O_2$. The phases present are an initial rhombohedral phase (H1) for $0.0 \leq x \leq 0.25$, a monoclinic phase (M) for $0.25 \leq x \leq 0.55$, a rhombohedral phase (H2) for $0.55 \leq x \leq 0.75$, and finally two coexisting phases (H2 + H3) for $0.75 \leq x \leq 1$. The last H2 ↔ H3 phase transition at around 4.2 V is believed to be mainly responsible for capacity fade, and this capacity fade is closely related to both the extent and reversibility of the H2 ↔ H3 phase transition.[14,15,18,31-33] The intensity of the peak corresponding to the H2 ↔ H3 phase transition for the CC90 cathode is initially higher than that for the CSG90 cathode and gradually decays and polarizes with cycling, indicating that the original layer structure is slowly undermined by the cyclic compressive/tensile strain arising from the H2 ↔ H3 phase transition. In comparison, the dQ dV^{-1} profiles of the CSG90 cathode hardly change, confirming the excellent reversibility of the H2 ↔ H3 transition and the resultant structural stability. To explicitly demonstrate the impact of the H2 ↔ H3 phase transition on the unit cell dimensions, *in-situ* XRD analysis was performed while charging the cathodes to 4.5 V (1st cycle) at a constant current density of 40 mA g^{-1}. Figure S5 show a series of (003) reflections, which directly evidence the *c*-axis lattice parameter variation, and (110) reflections, which directly evidence the *a*-axis lattice parameter changes. The (003) reflections for both CC90 and CSG90 cathodes shift to lower angles when charged to 4.1 V as the unit cells for both cathodes expand in the *c*-direction, likely from the coulombic repulsion of the anion layers. Beyond 4.1 V, the unit cells for the two cathodes begin to contract.

However, both the shape and position of the (003) reflections for the two cathodes differ increasingly significantly as charging proceeds. The nearly symmetric shape of the (003) reflections beyond 4.1 V indicates that the CC90 cathode remains as a single phase, implying that the transformation from the H2 to the H3 phase occurs rather abruptly. Conversely, the (003) reflections for the CSG90 cathode contain a broad shoulder, indicating the simultaneous presence of multiple phases. Meanwhile, the (110) reflection continuously shifts to a higher angle and plateaus at ≈4.2 V for both cathodes. In order to better trace the phase evolution above 4.1 V in the two cathodes, the deconvoluted (003) reflections as a function of the state of charge were obtained, as shown in **Figure 3**. The deconvoluted (003) reflections for $Li_{1-x}[Ni_{0.95}Co_{0.025}Mn_{0.025}]O_2$ obtained from a similar *in situ* experiment are also shown for comparison. The deconvoluted (003) reflections for the CC90 cathode indicate that it is completely converted from H2 to H3 above ≈4.2 V and the co-existence of two phases is only detected around 4.2 V (Figure 3a). Hence, the phases before and after the transition are sharply defined, and this sharp phase transition results in an abrupt decrease in the *c*-axis lattice parameter. In the case of the CSG90 cathode, the H3 phase begins to appear above 4.2 V as the Li is removed from the cathode. However, this phase emerges at a much slower rate than that observed for the CC90 cathode. Unlike in the CC90 cathode, the H2 phase persists up to 4.5 V in the CSG90 cathode (Figure 3b). A similar phase transition from H3 to O1 is also observed for the single-composition $Li_{1-x}[Ni_{0.95}Co_{0.025}Mn_{0.025}]O_2$ cathode in the deeply charged state.[18,34,35] Similar to the CSG90 cathode, the two phase transitions (H2 → H3 and H3 → O1) in $Li_{1-x}[Ni_{0.95}Co_{0.025}Mn_{0.025}]O_2$ are also sharply demarcated (Figure 3c). The co-existence of O1, H3, and H2 phases in the CSG90 cathode is attributed to the simultaneous presence of discrete regions containing different Ni contents. The appearance of the O1 phase is due to the core region with its composition close to $Li_{1-x}[Ni_{0.94}Co_{0.0038}Mn_{0.022}]O_2$, and the prolonged coexistence of the H2 and H3 phase is caused by the concentration gradient region in the outer shell layer having an Ni content ranging from 84% to 94% within a single CSG90 particle (Figure S6). The protracted phase transition (H2 → H3) lasting up to the end of charging observed in the CSG90 cathode, unlike the abrupt phase transitions in the CC90 and $Li[Ni_{0.95}Co_{0.025}Mn_{0.025}]O_2$ cathodes, is a unique feature effected by the non-uniform spatial distribution of Ni ions, the concentration of which dictates the extent of the phase transition.

Figure 3d and 3e summarize the *a*- and *c*-axis lattice parameters obtained from the *in-situ* XRD data for the CC90 and CSG90 cathodes during charging. The *a*-axis lattice parameter for both cathodes progressively decreases from 2.87 to 2.81 Å at 4.2 V and stabilizes as the Li ions are further removed such that the maximum Δa is -2.1%, which is consistent with previously reported result.[14,15] In comparison, the change in the *c* lattice parameter is more drastic and differs between the two electrodes. The *c*-axis lattice for the CC90 cathode decreases from 14.4186 Å at 4.0 V ($x = 0.58$ in $Li_{1-x}[Ni_{0.90}Co_{0.05}Mn_{0.05}]O_2$) to 13.6129 Å at 4.5 V ($x = 0.90$), which corresponds to maximum Δc of -5.6%, as shown in Figure 3e. The *c*-axis lattice parameter for the H2 phase in the CSG90 cathode decreases by 2.8% (from 14.3978 Å at 4.0 V to 13.9959 Å at 4.5 V). The appearances of the H3 and O1 phases incur 4.9% and 6.2% contractions in the *c*-axis, respectively, since the lattice parameters decrease to 13.6999 Å and 13.5013 Å at 4.5 V for the H3 and O1 phases, respectively. Although the maximum Δc for the CSG90 cathode is larger than that of the CC90 cathode at charge end because of the formation of the O1 phase, the average *c*-axis contraction of the CSG90 cathode is only 5.1% based on the average weight fractions of the H2, H3, and

O1 phases, i.e., 13.7%, 49.5%, and 36.8%, respectively. Therefore, the average volume expansion/contraction of the CSG90 cathode is effectively less than that of the CC90 cathode, despite the fact that the core region, which comprises the bulk of the CSG90 particle, has a Ni content higher than that of the CC90 cathode. It appears that the encapsulating CG shell layer partially suppresses the detrimental phase transition near the charge end and also blunts the abrupt dimensional change by protracting the phase transition to the charge end. Moreover, the relatively stable outer surface of the CSG90 cathode not only prevents the microcrack formation, it also prohibits liquid electrolyte penetration to the particle interior, thus reducing the subsequent degradation of the exposed surfaces by the electrolyte.[14,15,28,36]

To confirm the coexistence of multiple phases in a charged CSG90 cathode particle, a CSG90 cathode charged to 4.5 V was examined using TEM after a relaxation period of 20 h. Figure S7a shows a bright field TEM image of a primary particle located at a secondary particle surface. The corresponding electron diffraction pattern in Figure S7b approximately matches the 100 zone axis of the prototype layered structure found in $LiCoO_2$ or $LiNiO_2$ but contains overlapping diffraction spots and streaks, which likely indicates stacking faults.[37,38] Therefore, the surface primary particles in the CSG90 cathode are composed of regions with different but similar crystal structures (e.g., H2 and H3). The selected area electron diffraction (SAED) pattern from a primary particle selected from the approximate center of a secondary particle that was fractured was indexed to the 100 zone of a spinel structure ($Fd\bar{3}m$) (Figure S7c and S7d). The spinel structure is typically produced in deeply charged Ni-rich NCM cathodes as Ni ions migrate to the Li layer and occupy the vacant sites due to their similar ionic radii.[39] In the case of the primary particle near the center, the entire particle, which is highly enriched in Ni, is transformed from the original layered structure to the spinel structure.

Thus, an array of different crystal structures ranging from H3, H2, and O1 to $Fd\bar{3}m$ are observed depending on local composition, as inferred from the XRD data.

It should also be noted that the lattice contraction resulting from the appearance of the H3 phase is highly anisotropic since Δa = -2.1 % whereas Δc is as high as -6%. As shown by the TEM analysis below, the two cathodes have strikingly dissimilar microstructures, which also play roles in relieving the mechanical stress caused by lattice contraction. The strong crystallographic texture observed in the CG shell layer of the CSG90 cathode material orients the c-axis of the encapsulating primary particles along the radial direction of the secondary particle so that the internal strain arising from the lattice contraction is uniformly distributed without localized build-up of mechanical stresses. In the CC90 cathode, which comprises randomly oriented primary particles, the anisotropic lattice contraction can lead to regions, especially along the interparticle boundaries, with high stress concentrations, further aggravating the destabilization of the mechanical integrity of the CC90 cathode particles in the deeply charged state.

The effect of the superior mechanical stability of the CSG90 cathode is clearly observed in the cross-sectional SEM images of the CC90 and CSG90 cathodes during charging (4.19 V and 4.3 V) and discharging (4.16 V and 2.7 V) (**Figure 4**). The charged CC90 cathode particles starts to develop microcracks at the peak of the H2 → H3 phase transition. At 4.3 V (full charge), the microcracks grow to a fissure at the center with numerous subsidiary microcracks along the interparticle boundaries emanating from the center to the surface. In comparison the cracks nucleated at the center of the CSG90 particle at 4.19 V do not grow in size or in length and remain comparatively narrow at the fully charged state. Furthermore, the density of the microcracks, if any, is visibly lower in the CSG90 cathode at 4.3 V than in the CC90 cathodes. In addition, the microcracks in the CC90 cathode that reach the surface allow electrolyte infiltration to the particle core and such microcracks are not observed in the CSG90 cathode. Interestingly, the microcracks observed in both cathodes at 4.3 V gradually close back during discharging. The extent of this repeated opening and closing in the CC90 cathode is, however, apparently large enough to produce a permanent structural damage to the material. The microstructure of the CSG90 cathode at charge end unequivocally demonstrates the effectiveness of the CG shell layer in protecting the core region, which is extremely Ni-enriched, from nucleating microcracks, electrolyte infiltration, and eventual fracture failure of the cathode.

To demonstrate that the efficacy of the compositional partitioning is preserved during long term cycling, the two cathodes were cycled in pouch-type full cells containing graphite anodes (**Figure 5a**). The CC90 cathode retains only 68% of its initial discharge capacity while the CSG90 retains 88% of its initial capacity, confirming the superior cycling stability of the CSG90 cathode. This is especially important considering that an EV battery is required to maintain in excess of 80% of its initial capacity during service life. To correlate the long-term cycling stability with the microstructural damage sustained by each cathode during cycling, the cycled cathodes were recovered after 500 cycles and a thin section of each cycled cathode prepared using a focused ion beam was analyzed using TEM. The bright field STEM image of the cycled CC90 cathode in Figure 5b corroborates its inferior cycling stability, as several visible microcracks emanating from the particle center are observed. In addition to the large microcracks, interparticles have been separated by a thin gap which can be more clearly seen in the magnified dark field STEM image in Figure 5c. Apparently, the CC90 cathode is made up of relatively large primary particles (≈1 μm in width and length), allowing the microcracks to easily propagate along the interparticle boundaries. In contrast, the CSG90 cathode consists of much finer primary particles that are rather elongated in shape and arranged radially, extending in all directions from the particle center (Figure 5d). The fine primary particles absorb the cycling anisotropic strain and deflect the crack propagation, as evidenced by the lack of visibly large microcracks in the cycled CSG cathode (Figure 5e). Figure 5 demonstrates the stark contrast in internal microstructure between CC90 and CSG90 cathodes so that the CSG90 cathode not only achieves the intended protraction of the deleterious phase transition through compositional partitioning but also creates a microstructure conducive to relieving the anisotropic strain resulting from the phase transition and to deflecting microcrack propagation. An additional benefit of the CSG90 cathode is the crystallographic texture that develops in the CG shell layer. The image of the primary particle in the CS shell layer and its SAED pattern verify that the longitudinal axis of the elongated particle is aligned along the a-direction, which aligns the layer planes parallel to the radial direction (**Figure 6a**). The observed crystallographic texture distributes the resulting strain uniformly throughout the secondary particle because the unit cell expansion/contraction is mostly confined to the c-direction. As shown in the high-resolution image of a CSG90 primary particle surface exposed to electrolyte (Figure 6b), the damaged region, which is converted to a NiO-like rock-salt structure as evidenced by the accompanying Fourier transform (FT) images, is limited to a thickness of ≈5 nm. In comparison, the surface of the primary particle from the cycled CC90 cathode is composed of two regions: a ≈10-nm-thick surface region of the rock-salt structure and a≈20 nm-thick subsurface region of a heavily damaged layered structure containing numerous stacking faults and distorted layer planes (Figure 6c and 6d). The progressive change in the surface structure is illustrated by the FT images of the respective regions. As expected, because of the Ni-rich surface composition of the CC90 cathode, the surface damage of the cathode is more severe than that of the CSG90 cathode. In addition to surface damage, because of the electrolyte penetration in the CC cathode, the interior primary particle from the cycled CC90 cathode also presents severe surface damage (Figure 6e). The interior particle has a thick rock-salt layer (≈30 nm thick). Moreover, a polycrystalline layer, judging from several overlapping diffraction patterns, topped with an amorphous layer, is also observed on the outer surface of the interior primary particle. This damaged region, marked as III, is most likely an indication of material loss through dissolution (Figure 6f). Thus, TEM analysis provides convincing evidences that the CSG90 cathode preserves its mechanical integrity and protects its outer and internal surfaces from electrolyte attack during cycling. The set of SEM images graphically demonstrates the mechanical failure or non-failure of the two cathodes upon repeated Li insertion/removal for 1,000 cycles (Figure 6g-6j). In agreement with the TEM analysis, microcracks and particle fracture are observed in the CC90 cathode after only 500 cycles (Figure 6g). After 1,000 cycles, the CC90 cathode particles are nearly pulverized into individual primary particles (Figure 6h, S8a, and S8b). In comparison, no visible microcracks are observed for CSG90 after 500 cycles (Figure 6i) and only hairline cracks are observed after 1,000 cycles (Figure 6j, S8c, and S8d). Also, the compositional partition of CSG90 still remains unaffected by long-term cycling (Figure S9).

Furthermore, the improved chemical stability is clearly demonstrated by accelerated calendar testing in which the delithiated cathodes (charged to 4.3 V) were stored in the electrolyte used for cycling at 60 °C for an extended period. The stored electrodes were removed from the electrolyte at different intervals and cycled at 30 °C in a half cell using a Li metal anode. The initial discharge capacities of the CC90 and CSG90 cathodes are plotted against storage time in Figure S10a. Also included in the plot is the data for $Li[Ni_{0.8}Co_{0.1}Mn_{0.1}]O_2$ for comparison. The discharge capacities for all three cathodes decrease as the aging period increases, but the magnitude of the capacity loss is lowest for the CSG90 cathode. Although the CSG90 and $Li[Ni_{0.8}Co_{0.1}Mn_{0.1}]O_2$ cathodes have similar surface compositions, the CSG90 cathode minimizes the chemical damage in the charged state because of the absence of microcracks that provide channels for electrolyte infiltration. The capacity retention during the first 10 cycles, as shown in Figure S10b, confirms the outstanding chemical stability of the CSG90 cathode as nearly 190 mAh g^{-1} is maintained even after the cathode is exposed to the electrolyte at 60 °C for 15 days. Conversely, the capacity of the CC90 cathode is limited to 140 mAh g^{-1} after 15 days of exposure.

To directly confirm the superior mechanical stability of the CSG90 cathodes, the stress distribution within a single particle was calculated during the fully charged state based on the lattice parameter changes measured by XRD. The stress field inside a representative core/shell structure after charging (delithiation of the cathode) was calculated by a 2D finite element analysis using ANSYS 19.2a (Canonsburg, PA, USA). The individual core grains were drawn according to the microstructure acquired by TEM image (Figure 6a-f) and a random crystallographic orientation was assigned to each of the 355 core grains (**Figure 7a** and 7b). 144 shell grains were radially aligned so that all *a*-axis were orientated radially with respect to the shell circumference. Common edges between grains were treated as bond connections. The material properties used are summarized in Table S3. The lithiated cathode (discharged battery) was assumed to be stress free. After imposing the corresponding anisotropic strains, the stress field was calculated disregarding any plastic deformation which is sufficient to allow a comparison between a singular core structure a core shell structure and to see the principal effect of the shell. The calculated local tensile and compressive stress fields resulting from the anisotropic volume change of the primary particles are plotted in Figure 7c-f. Our simulation shows that, after delithiation (i.e. charged) of the CSG90 particles, the encapsulating shell compresses the core and leads to slightly smaller tensile stresses (σ_{tensile}) in the core than in the CC90 particles without the shell. Consequently, the compressive stresses (σ_{comp}) inside the core increase slightly in the presence of the shell. As tensile stresses tend to cause the nucleation of the microcracks during charging, the reduced level of tensile stress not only improves the mechanical integrity of the core but also suppresses the microcrack formation. Even more importantly, the shell exhibits a much more homogeneous stress field significantly smaller in magnitude compared to the maximum values of the shell-free core (CC90 particles) which, together with the highly aligned geometry of the shell, suppresses the crack growth inside the shell. For more than a decade, our group has systematically developed CSG cathode materials. These composition-controlled cathode materials outperform the single composition cathode especially in cycling performance and thermal stability and this tendency is more pronounced with increasing Ni content ($x > 0.9$). **Figure 8** shows the radar summary chart comparing the overall performance comparison of the single composition cathodes with dashed lines and the CSG cathodes with solid lines. A high energy density can be potentially achieved by highly Ni-enriching the NCM cathodes to meet the drive-range of threshold 300 miles but only the CSG cathodes exhibit superior electrochemical performances and thermal stability that are compatible for EV applications. Comparing the two CSG cathodes (CSG90: current work, CSG95), the CSG90 cathode provides better cycling stability at an elevated temperature (60 °C), and better thermal stability (hence, safer battery) (Figure 8, S4, and Table S2) compared to the CSG95 cathode.[27] A slightly higher discharge gained by the CSG95 cathode is clearly outweighed by the better thermal stability and the high-temperature cycling stability exhibited by the CSG90 cathode as can be seen in Figure 8. These outstanding thermochemical and structural stability of the CSG90 cathode are attributed to the more elongated primary particle than those of the CSG95 cathode and the compact structural geometry (Figure S11). In addition, the higher Co and Mn concentrations in the encapsulating shell layer protect the cathode surface from electrochemical side reactions. (Figure S12).

Conclusion

We have demonstrated that the unique compositional and spatial configuration of the CSG90 cathode can dissipate the internal stains generated by the detrimental H2 ↔ H3 phase transition that occurs in Ni-enriched NCM cathodes in the deeply charged state. This markedly improves cycle performance as well as thermochemical stability as schematically summarized in **Figure 9**. We believe that our strategy of compositional partitioning of cathode particles and subsequent optimization of their microstructural response to internal strain may lead to the rational design and development of a wide range of multi-functional cathodes, especially Ni-rich NCM cathodes.

Experimental Section

Synthetic procedures: Spherical $[Ni_{0.9}Co_{0.05}Mn_{0.05}](OH)_2$ precursor was synthesized via a co-precipitation method with $NiSO_4 \cdot 6H_2O$, $CoSO_4 \cdot 7H_2O$, and $MnSO_4 \cdot H_2O$ aqueous solution as a starting material. A solution (Ni:Co:Mn = 90:5:5 in molar ratio) was pumped into a batch reactor (47 L) containing a solution of NaOH (aq.) and NH4OH (aq.) under a N_2 atmosphere. Simultaneously, 4.0 mol L^{-1} of NaOH (aq.) and 10.5 mol L^{-1} of NH_4OH (aq.) were also pumped into the reactor. During synthesis, initially formed $[Ni_{0.9}Co_{0.05}Mn_{0.05}](OH)_2$ particles became spherical under vigorous stirring. The final precursor powder was obtained through washing, filtration, and vacuum drying at 110°C for 12 h. To obtain CC90, the precursor $[Ni_{0.9}Co_{0.05}Mn_{0.05}](OH)_2$ was mixed with $LiOH \cdot H_2O$ (Li:(Ni+Co+Mn) = 1.01:1 molar ratio) and calcined at 750°C for 10 h under oxygen atmosphere.

To prepare Spherical CSG $[Ni_{0.9}Co_{0.05}Mn_{0.05}](OH)_2$ precursor via co-precipitation, 2.0 mol L^{-1} of $NiSO_4{\cdot}6H_2O$ aqueous solution was used as a starting material for the core composition of $Ni(OH)_2$. The $NiSO_4{\cdot}6H_2O$ aqueous solution was continuously fed into a batch reactor (47 L) containing a solution of NaOH (aq.) and NH_4OH (aq.) under a N_2 atmosphere. Simultaneously, 4.0 mol L^{-1} of NaOH (aq.) and 10.5 mol L^{-1} of NH_4OH (aq.) were also pumped into the reactor. During synthesis, initially formed $Ni(OH)_2$ particles became spherical under vigorous stirring. Then, in order to construct the core-shell (CS) structure, a Ni-deficient aqueous solution of $NiSO_4{\cdot}6H_2O$, $CoSO_4{\cdot}7H_2O$, and $MnSO_4{\cdot}H_2O$ (Ni:Co:Mn = 8:1:1 molar ratio), corresponding to the shell composition of $[Ni_{0.8}Co_{0.1}Mn_{0.1}](OH)_2$, was introduced into the reactor. The obtained CSG $[Ni_{0.9}Co_{0.05}Mn_{0.05}](OH)_2$ powders were washed, filtered, and dried under vacuum at 110°C for 12 h. To obtain CSG 90, the precursor (CSG $[Ni_{0.9}Co_{0.05}Mn_{0.05}](OH)_2$) was mixed with $LiOH{\cdot}H_2O$ (Li:(Ni+Co+Mn) = 1.01:1 molar ratio) and calcined at 730 °C for 10 h under oxygen atmosphere.

Materials characterization: The chemical compositions of the prepared powders were determined by inductively coupled plasma (ICP, OPIMA 8300, Perkin Elmer). For detailed structural analysis, XRD patterns of the as-synthesized powder samples were obtained using synchrotron XRD on the 9B-HRPD beamline (λ = 1.51720 Å) at Pohang Accelerator Laboratory (PAL) in Pohang, Korea. Synchrotron XRD data were collected at room temperature with a six-multi detector system over the 2θ range 10−130° at a 0.02° step width. The structural refinement was performed by Rietveld analysis using the Fullprof suite. In situ XRD experiments were performed at the 5A MS-XRS beamline at PAL in Pohang, Korea. The wavelength (λ = 0.692650 Å) of the incident beam and the sample-to-detector distance were calibrated using a LaB6 standard. A modified 2032 coin-type half-cell with a 3 mm diameter hole at its center containing a kapton window served as the X-ray beam path. While the cell was being charged by applying a constant current of 36 mA g^{-1}, the XRD patterns were continuously recorded every 3.5 min with a 2D image plate (mar345) in transmission mode. The 2θ angles for all *in-situ* XRD patterns were converted to those of a conventional X-ray tube with λ = 1.5406 Å (Cu Kα radiation) for easy comparison. The morphologies and structures of the prepared particles were observed by scanning electron microscopy (SEM, Nova Nano SEM 450, FEI). For observation of the cross-section of the cathode particles by SEM, the recovered cathodes of different states were rinsed immediately using dimethyl carbonate and then completely dried under vacuum in a Ar-filed glovebox. The electrodes were cut using a cross-sectional polisher (CP, JEOL SM-09010). For the TEM samples, a particle collected from the 500th cycled electrode at the discharged state was cut into a 100 nm thick thin foil using a focused ion beam (FIB, JEOL 2100F) and loaded onto a Mo grid.

Electrochemical test: For the fabrication of the positive electrodes, the synthesized powders were mixed with carbon black and poly(vinylidene fluoride) (PVdF) (90:5.5:4.5 by weight percent) in *N*-methylpyrrolidone (NMP). The obtained slurry was coated on Al foil with an active material loading level of 4 - 5 mg cm^{-2}, roll-pressed, and vacuum dried. The electrolyte solution was 1.2 mol L^{-1} $LiPF_6$ in ethylene carbonate-ethyl methyl carbonate (EC:EMC=3:7 by volume) with 2 wt% vinylene carbonate (VC). Preliminary cell tests were performed with a 2032 coin-type half-cell using lithium metal as the anode. The cells were charged and discharged by applying a constant current density of 90 mA g^{-1} (0.5 C) between 2.7 and 4.3 V. Long-term cycling performances testing was performed in a laminated-pouch-type full-cell, using the Mesocarbon microbead (MCMB) graphite (Osaka Gas) as an anode, and 1.2 mol L^{-1} $LiPF_6$ in ethylene carbonate-ethyl methyl carbonate (EC:EMC=3:7 by volume) with 2 wt% vinylene carbonate (VC). A full-cell capacity balance (N/P ratio) was in the range of 1.15-1.20. The cells were charged and discharged between 3.0 and 4.2 V by applying a constant 1 C current density (200 mA g^{-1}) at 25 °C. In order to examine the degradation of cathodes during storage, an accelerated calendar aging test was devised. Each cathode was removed from the fully charged coin cell after a first formation cycle at 0.1 C-rate. The electrode was placed in a polytetrafluoroethylene (PTFE) bottle with an excess amount of electrolyte (20 mL) in an Ar-filled glove box and stored in chamber at 60 °C. To avoid contamination by the surrounding factors, the PTFE bottle was handled in the glove box and stored with vacuum packing. After calendar aging, each cathode was rinsed several times with fresh electrolyte and assembled into a coin cell using fresh components for the electrochemical test (0.1 C-rate).

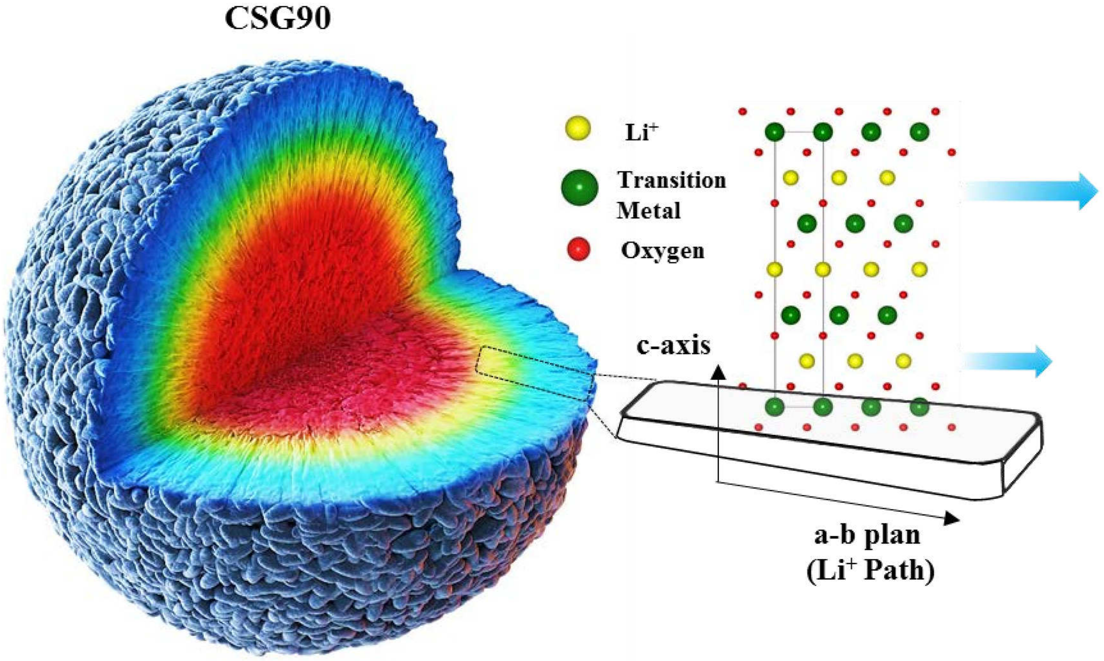

Figure 1. Schematic diagram of CSG particle with Ni-rich core surrounded by compositional partitioning outer layer.

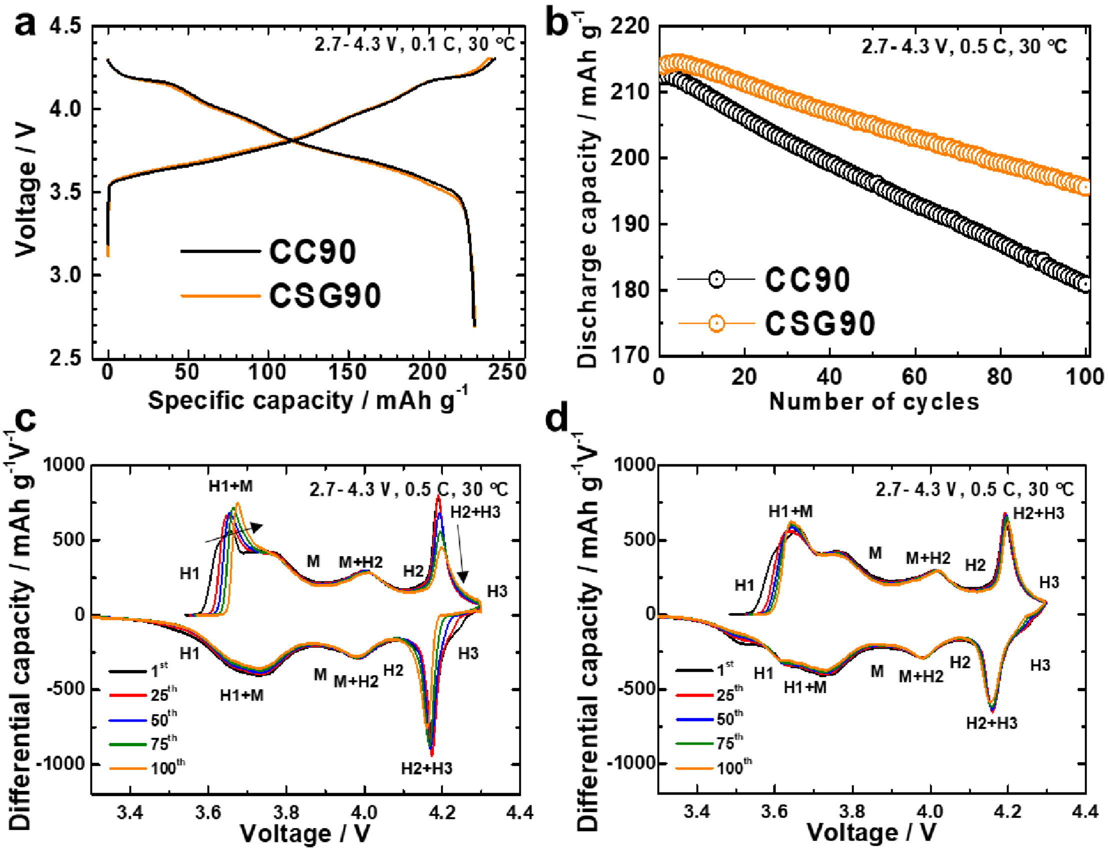

Figure 2. a) Initial charge and discharge curves at 0.1 C and 30 °C cycled between 2.7 and 4.3 V with a 2032 coin-type half-cell using a Li metal anode b) Cycling performances at 0.5 C of CC90 and CSG90; dQ dV^{-1} profiles as a function of the number of cycles for c) CC90, and d) CSG90 (H = hexagonal and M = monoclinic structures).

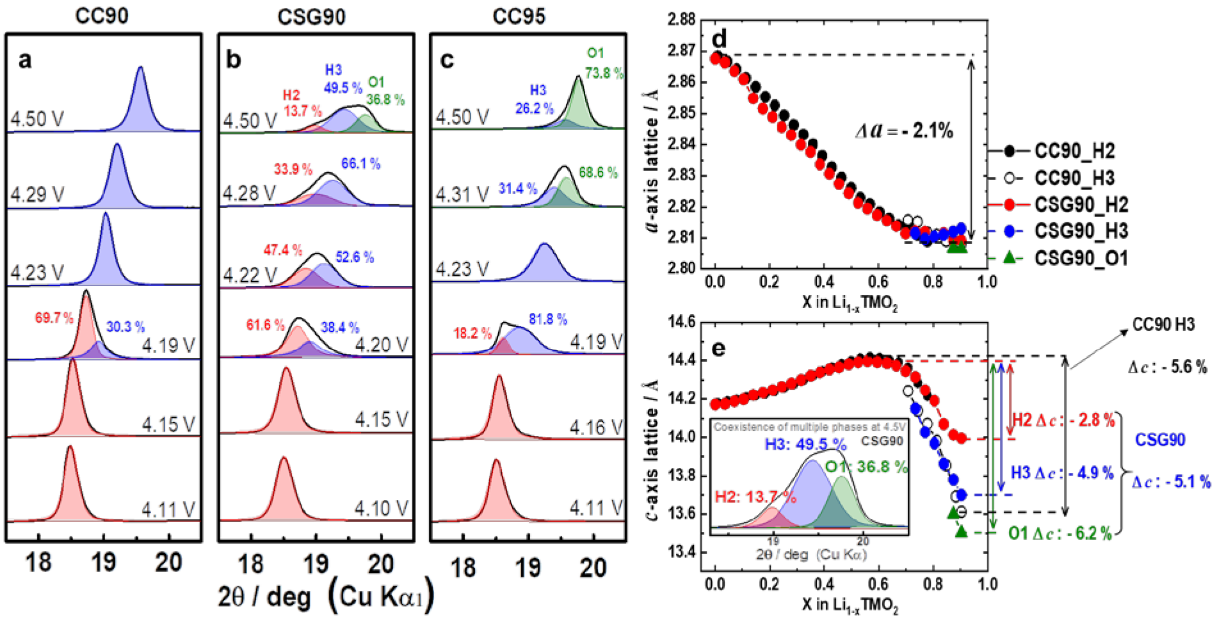

Figure 3. (003) reflections of a) CC90, b) CSG90, and c) CC95 ($Li_{1-x}[Ni_{0.95}Co_{0.025}Mn_{0.025}]O_2$) showing the coexistence phase ratio at each voltage. d) a-axis lattice parameters and e) c-axis lattice parameters of CC90 and CSG90 as a function of the amount of lithium in the cathode.

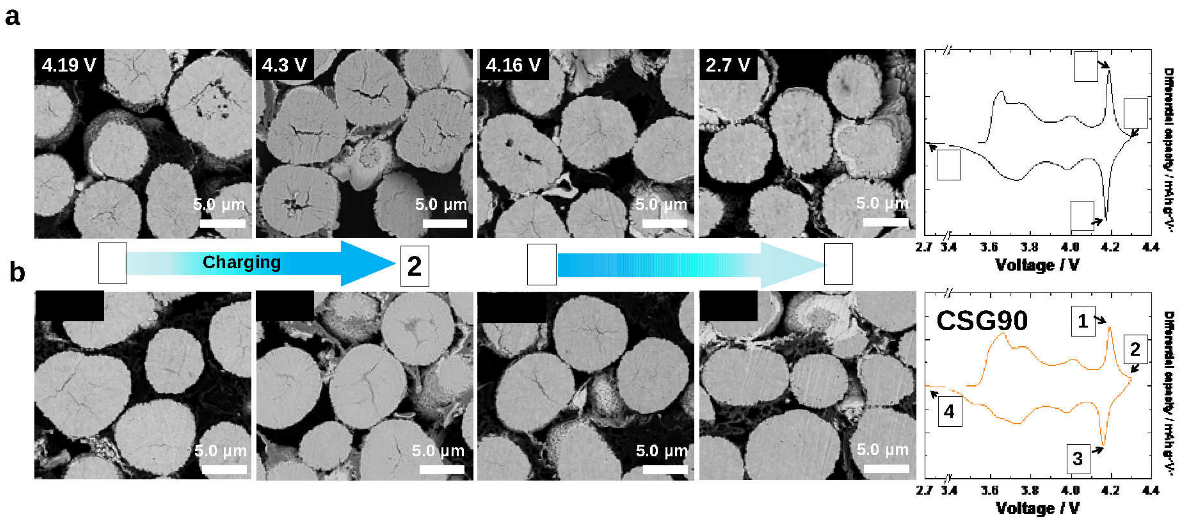

Figure 4. Cross-sectional SEM images of the 1st charge state at 4.19 and 4.3 V and discharge state at 4.16 and 2.7 V for a) CC90 and b) CSG90.

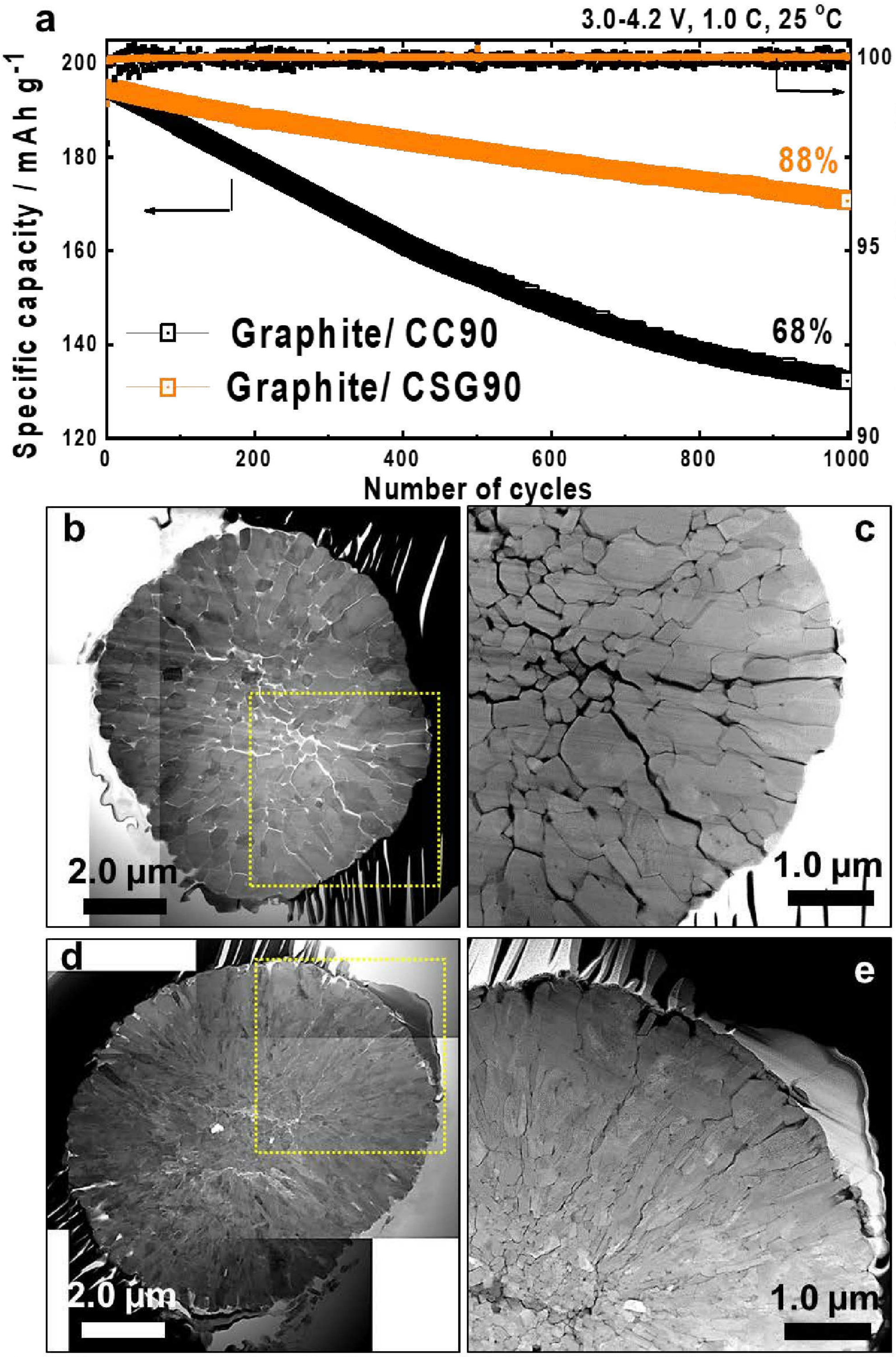

Figure 5. a) Long-term cycling performance of CC90 and CSG90 at 0.8 C charge/1.0 C discharge at 25 °C in pouch-type full cells using graphite as the anode. Mosaic scanning TEM images of cycled electrodes after 500 cycles using the full cell: b) CC90, c) magnified image of the area marked in b) by the yellow box, d) CSG90, e) magnified image of the area marked in d) by the yellow box.

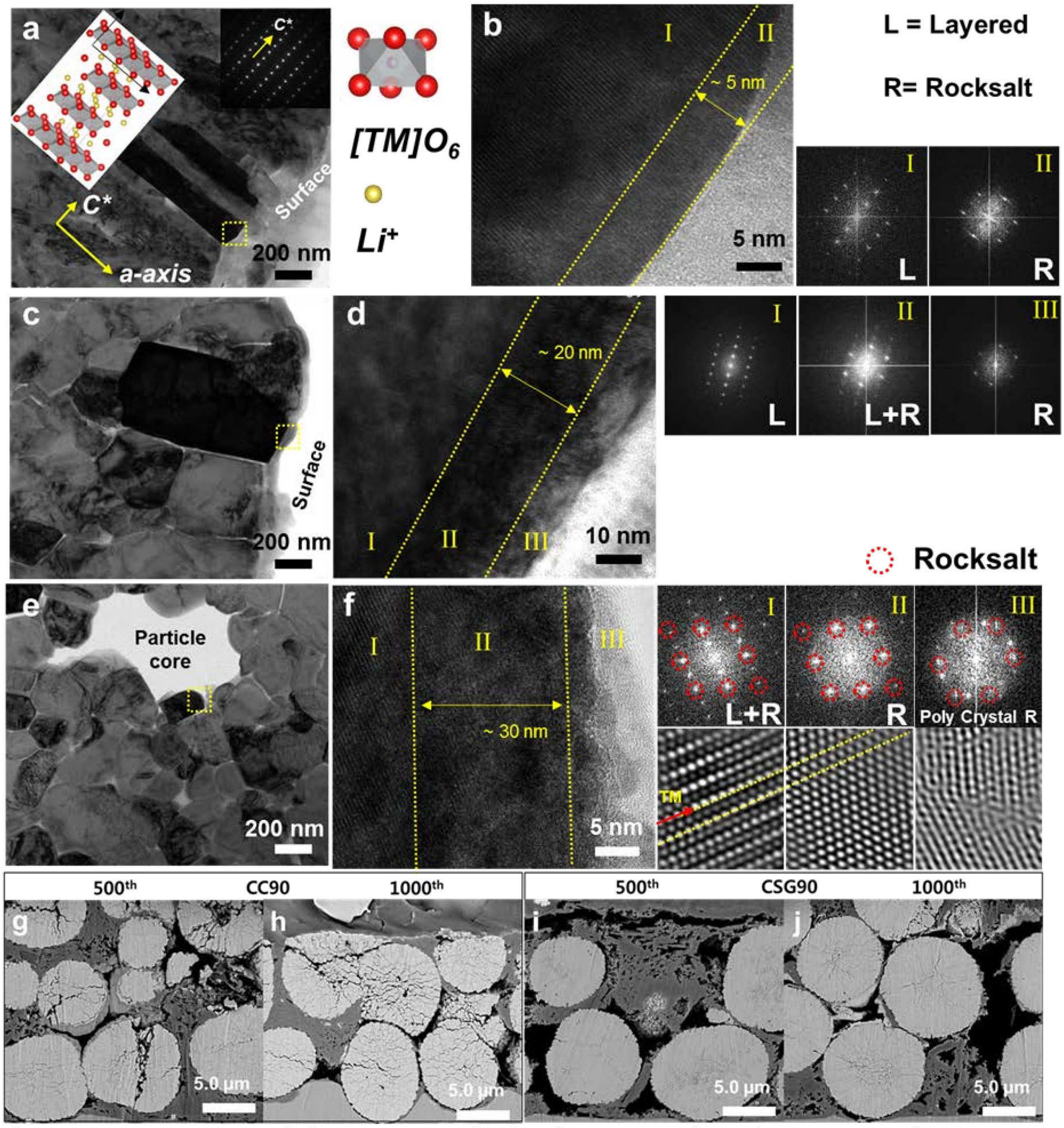

Figure 6. TEM image of the CSG90 cathode after 500 cycles: a) Low-magnification TEM images with the corresponding electron diffraction pattern (inset), b) high-magnification TEM images of the region marked by the yellow box in a), and Fourier filtered transforms of the regions marked by numerals in b). TEM image of the CC90 cathode after 500 cycles: c) particle surface and e) particle core low-magnification TEM images, d,f) high-magnification TEM images of the regions marked by yellow boxes in c,e), and Fourier filtered transforms of each region marked by numerals in d,f). Cross-sectional SEM images of discharge-state CC90 g) after 500 cycles, h) 1,000 cycles, CSG90 i) after 500 cycles and j) 1,000 cycles.

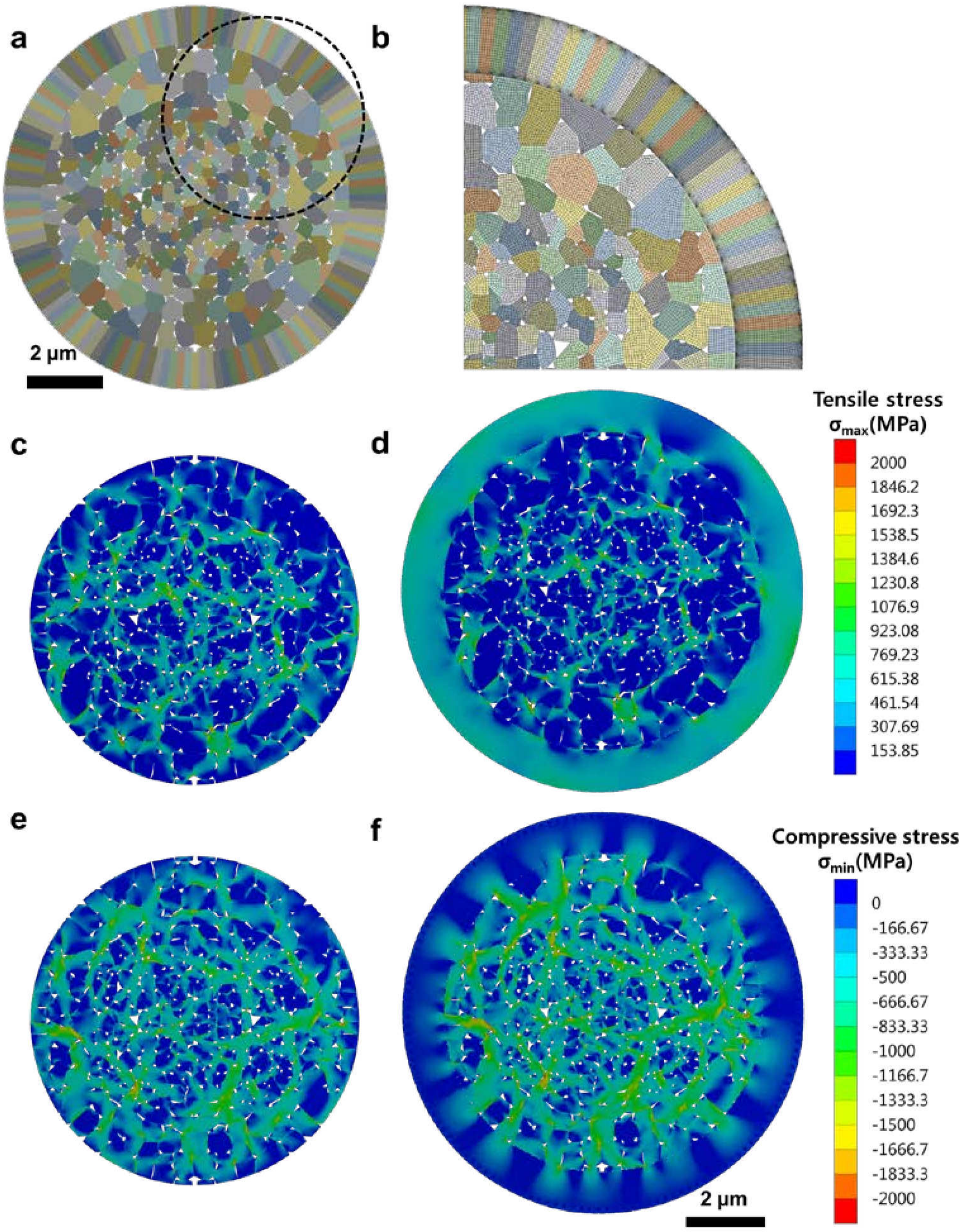

Figure 7. a) 2D model of core/shell particle and b) mesh for finite element analysis. Tensile stress for c) CC90 and d) CSG90 particles and compressive stress for e) CC90 and f) CSG90 particles (Max. Principal Stress) distribution after delithiation and lithiation.

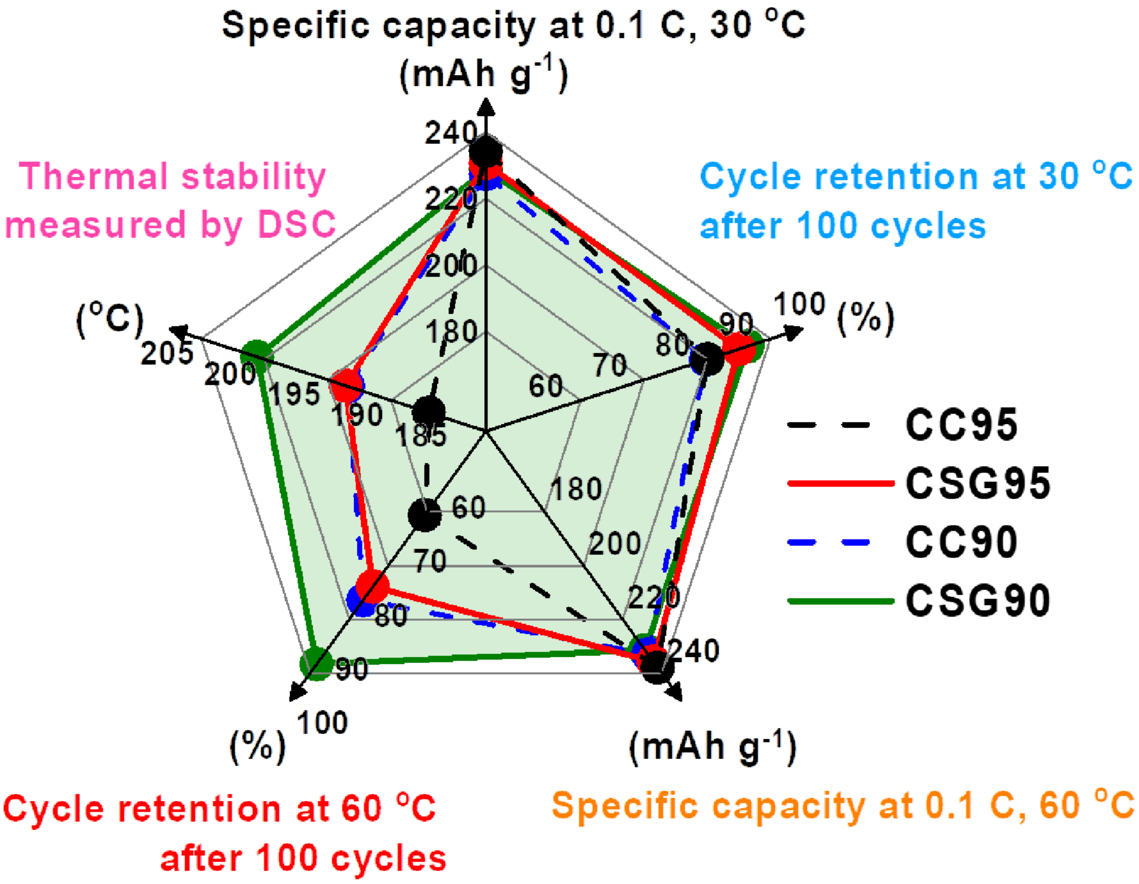

Figure 8. Radar summary chart displaying the performance comparison of the four cathode materials (CC95: single composition Li[$Ni_{0.95}Co_{0.025}Mn_{0.025}$]$O_2$, CSG95: double composition Li[$Ni_{0.95}Co_{0.025}Mn_{0.025}$]$O_2$).[25]

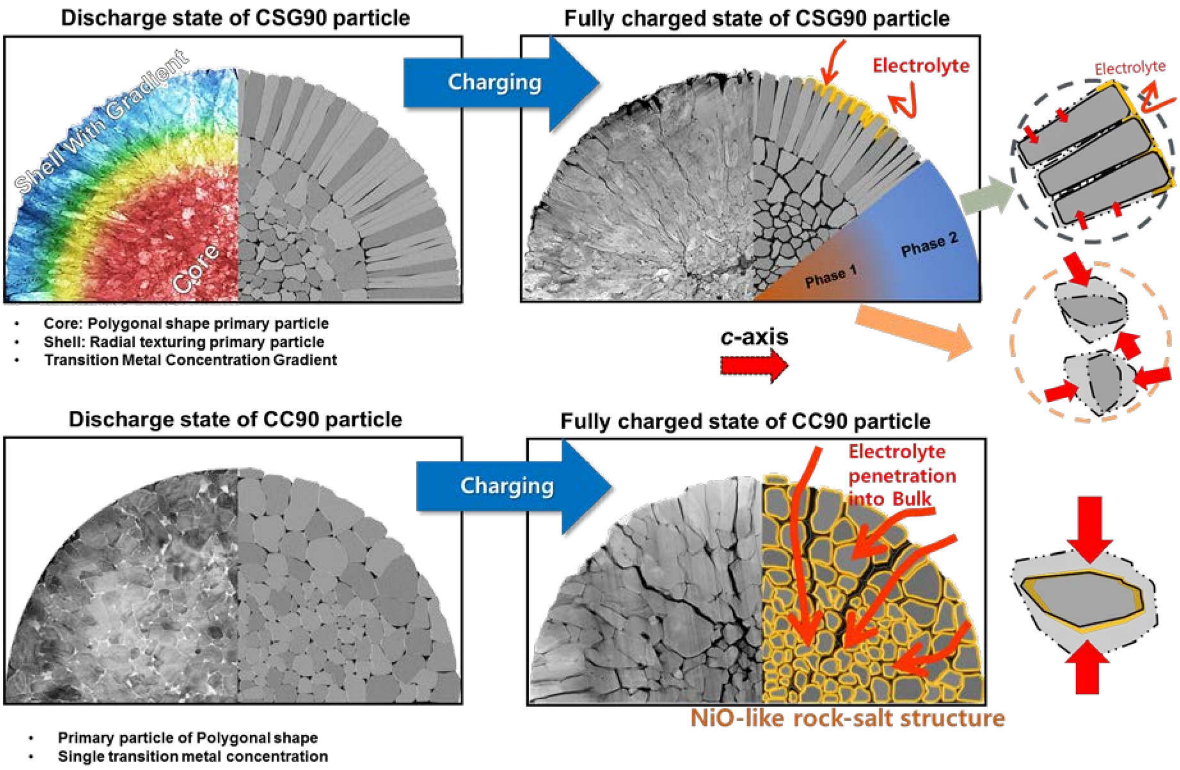

Figure 9. Schematic description of discharge and charge state. a) CSG90 and b) CC90 cathodes showing the internal morphological difference and the sustained damage.

Supporting Info

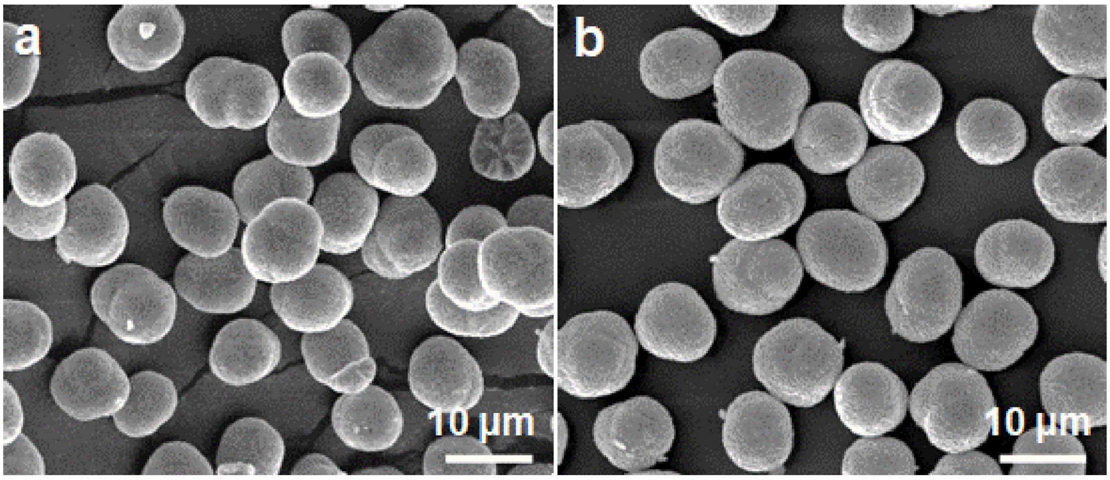

Figure S1. SEM images of as-prepared a) CC90 and b) CSG90 displaying their uniform spherical morphologies.

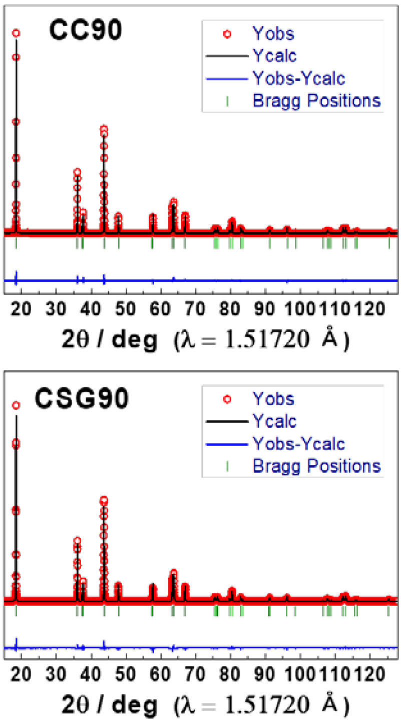

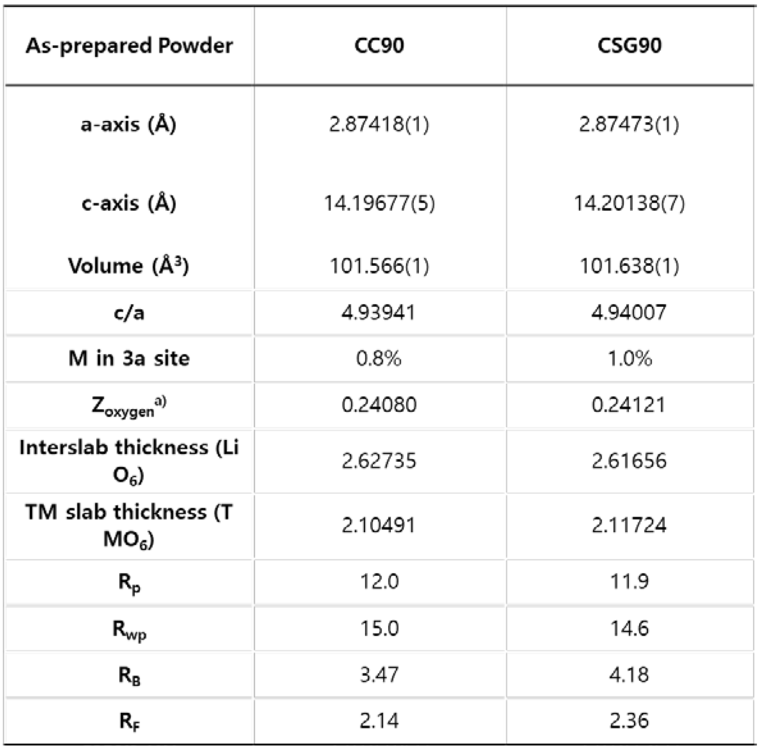

As-prepared Powder	CC90	CSG90
a-axis (Å)	2.87418(1)	2.87473(1)
c-axis (Å)	14.19677(5)	14.20138(7)
Volume (Å^3)	101.566(1)	101.638(1)
c/a	4.93941	4.94007
M in 3a site	0.8%	1.0%
Z_{oxygen}[a)]	0.24080	0.24121
Interslab thickness (LiO$_6$)	2.62735	2.61656
TM slab thickness (TMO$_6$)	2.10491	2.11724
R_p	12.0	11.9
R_{wp}	15.0	14.6
R_B	3.47	4.18
R_F	2.14	2.36

[a)] Z_{oxygen}: atomic coordinate for oxygen ions.

Figure S2. XRD patterns and Rietveld refinement of as-prepared CC90 and CSG90 cathodes.

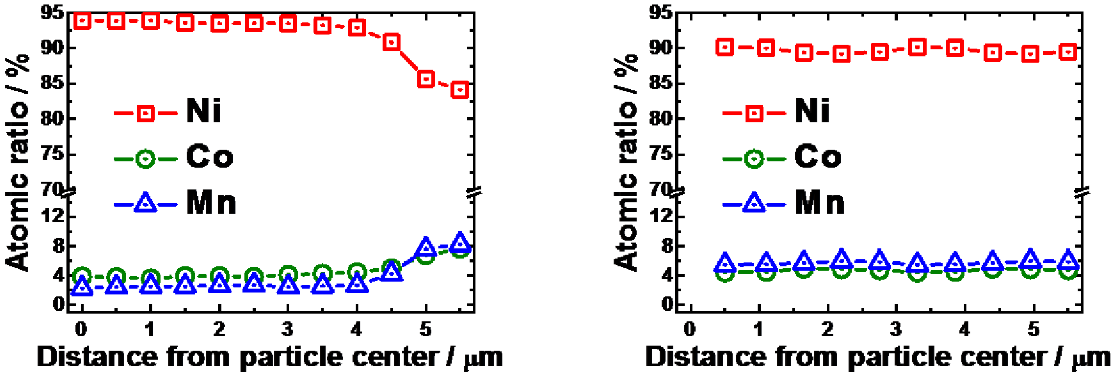

Figure S3. EPMA compositional scan across the a) CSG90 and the b) CC90 lithiated particle.

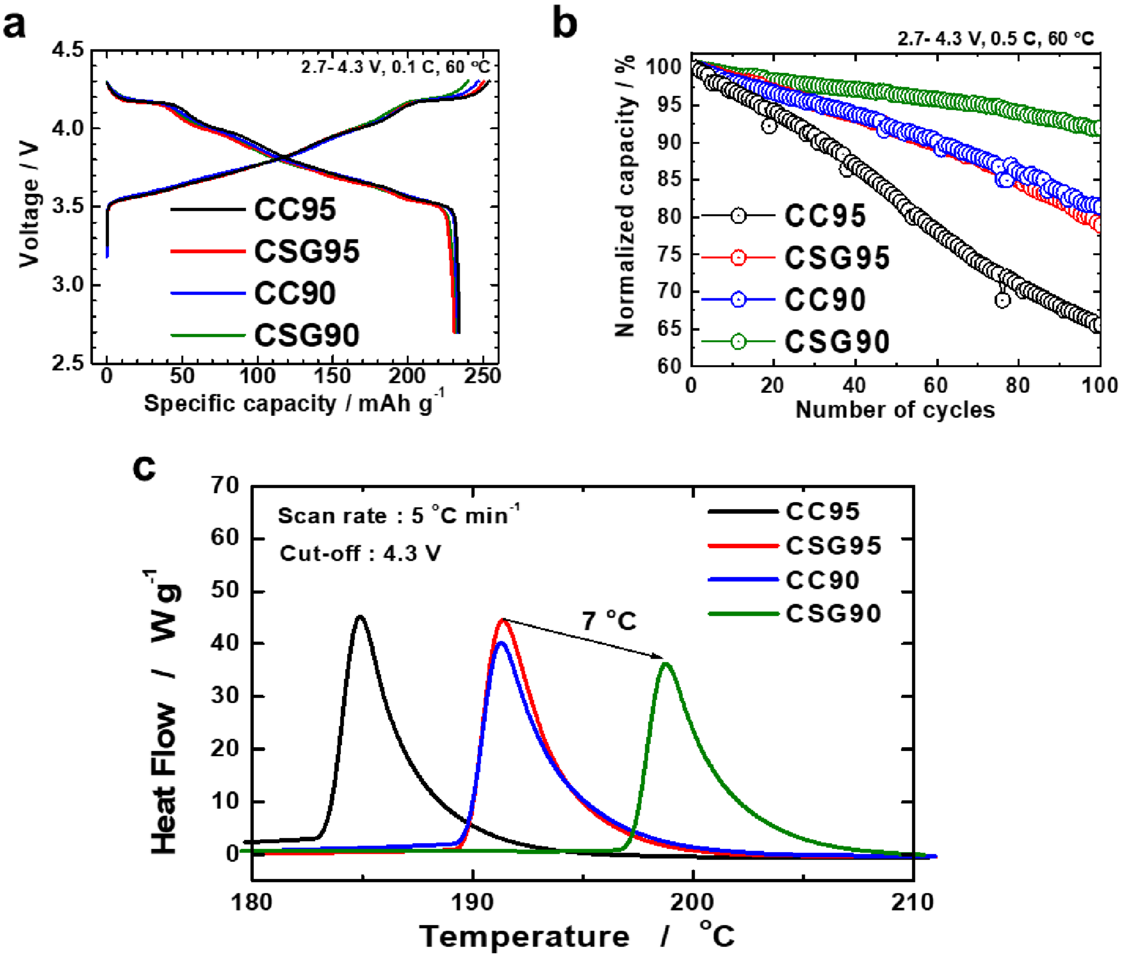

Figure S4. a) Initial charge and discharge curves at 0.1 C and 60 °C cycled between 2.7 and 4.3 V using 2032 coin-type half-cells with Li metal anodes; b) cycling performances at 0.5 C for CC95, CSG95, CC90 and CSG90. c) DSC profile of the CC95, CSG95, CC90 and CSG90 together with 1.2M $LiPF_6$, EC:EMC=3:7 by vol% + 2wt% VC electrolyte solutions.

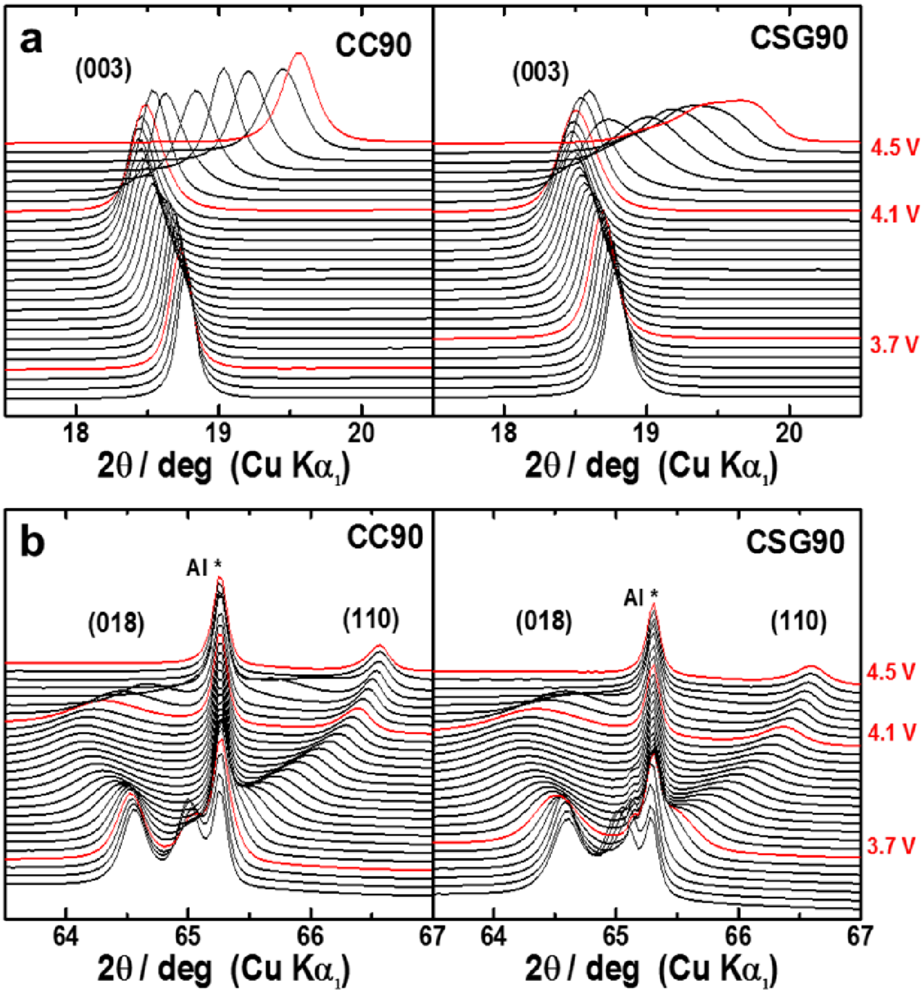

Figure S5. *In-situ* XRD patterns of CC90 and CSG90 in the 2θ ranges 17.7°–20.5° and 63.5°–67° for the a) (003) and b) (018) and (110) reflections during the 1st charge protocol.

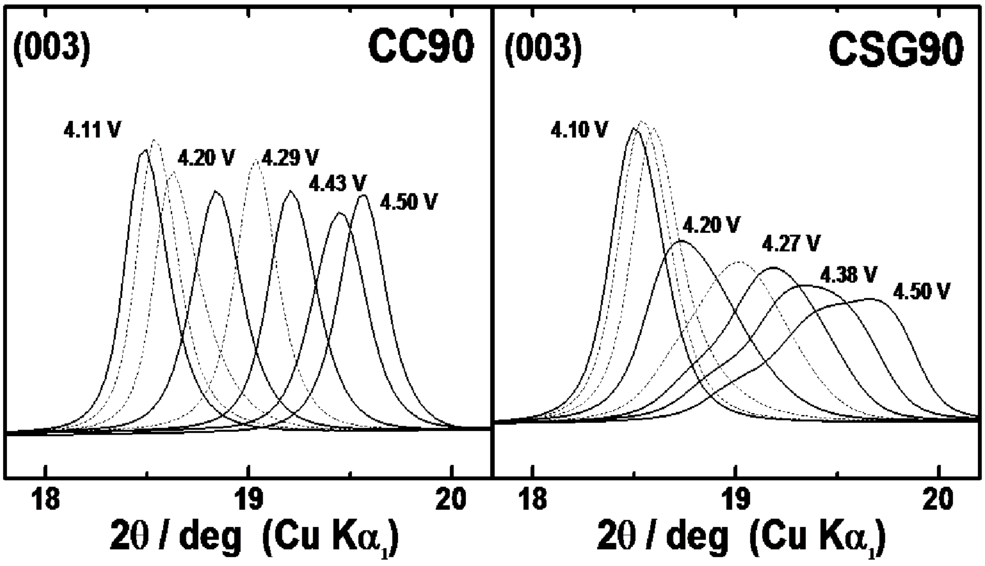

Figure S6. *In-situ* XRD patterns: (003) reflections for CC90 and CSG90 during the first charge process.

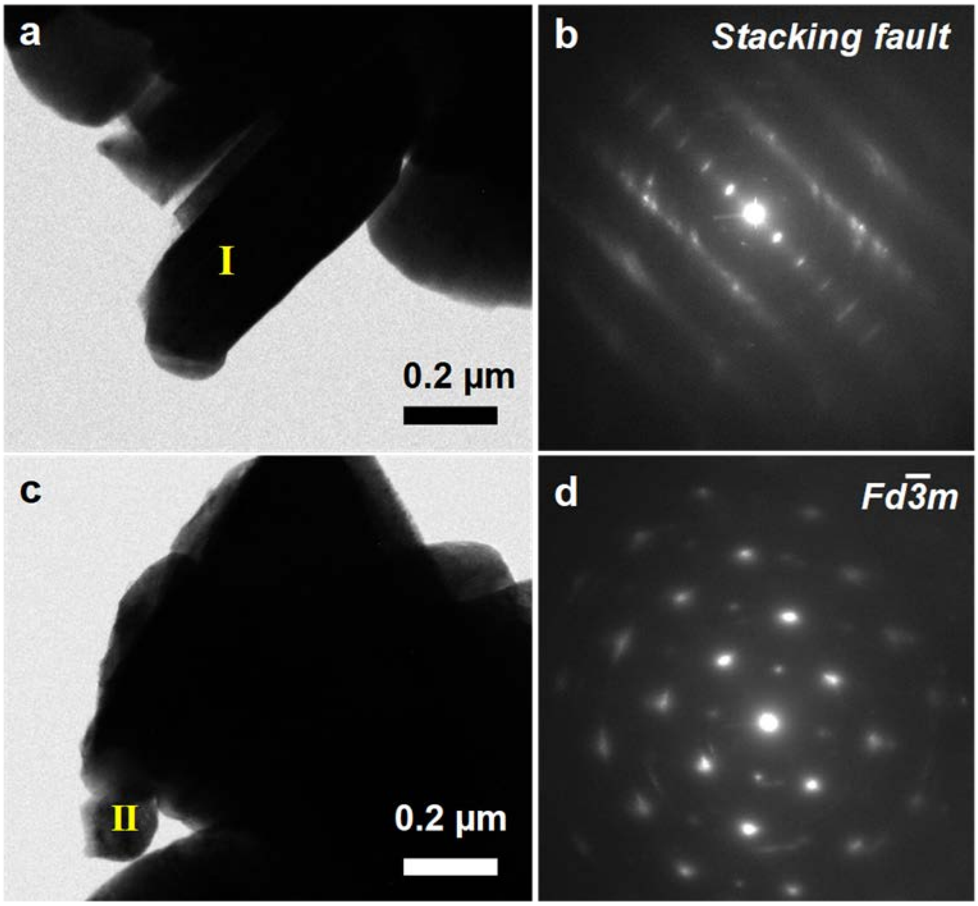

Figure S7. a) Bright-field TEM image of a primary particle located at the surface of the CSG90 cathode particle charged to 4.5 V and b) the electron diffraction pattern for the region marked I. c) bright-field TEM image of a primary particle at the center of the fractured CSG90 cathode particle charged to 4.5 V and d) the electron diffraction pattern for the region marked II.

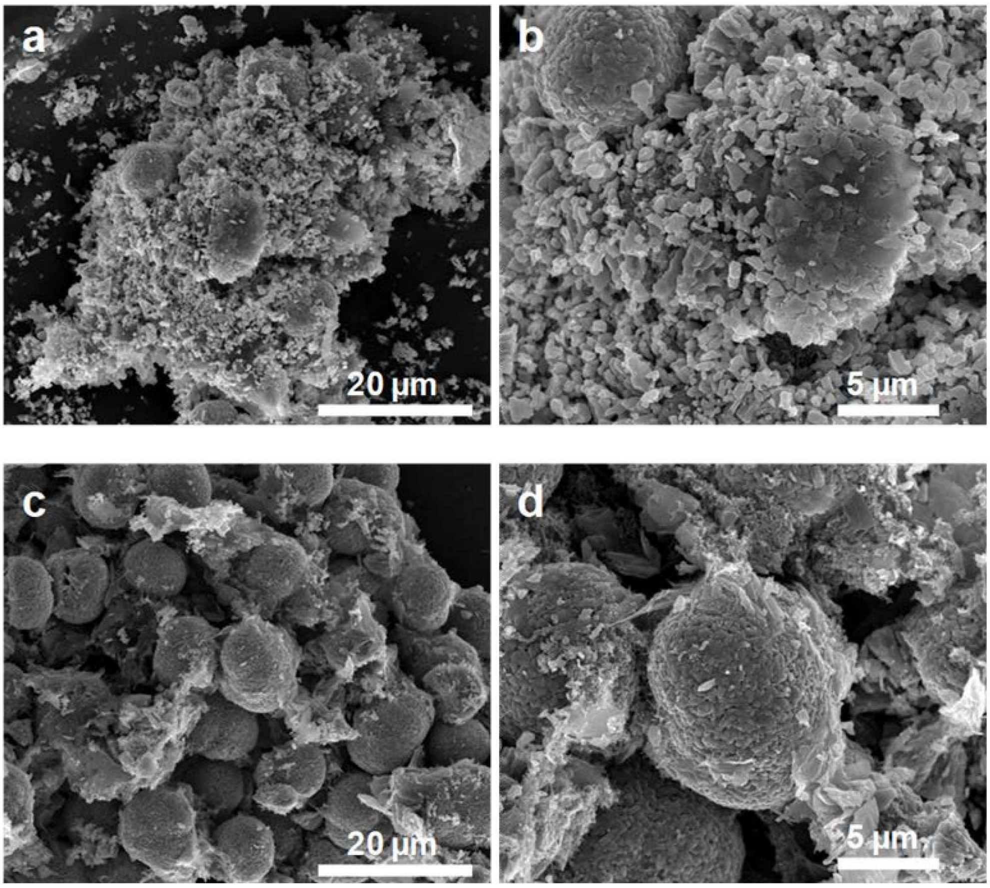

Figure S8. SEM images of cathodes after 1,000 cycles: Low-magnification SEM images of a) CC90 and c) CSG90. High-magnification SEM images of b) CC90 and d) CSG90.

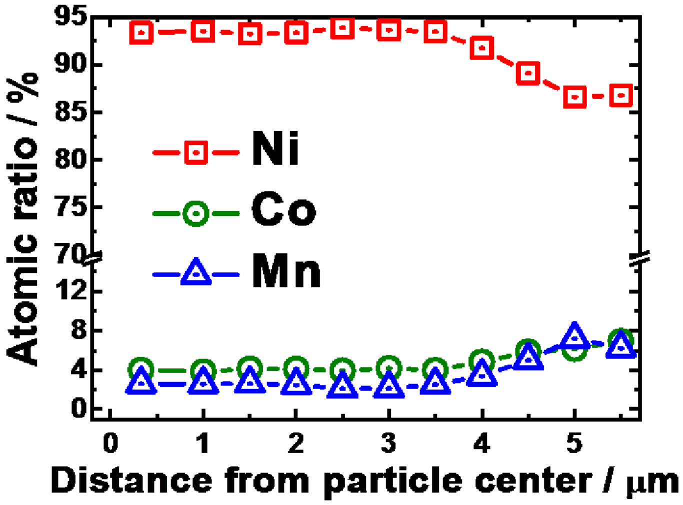

Figure S9. EPMA compositional scan across the 1000 cycled CSG90 lithiated particle.

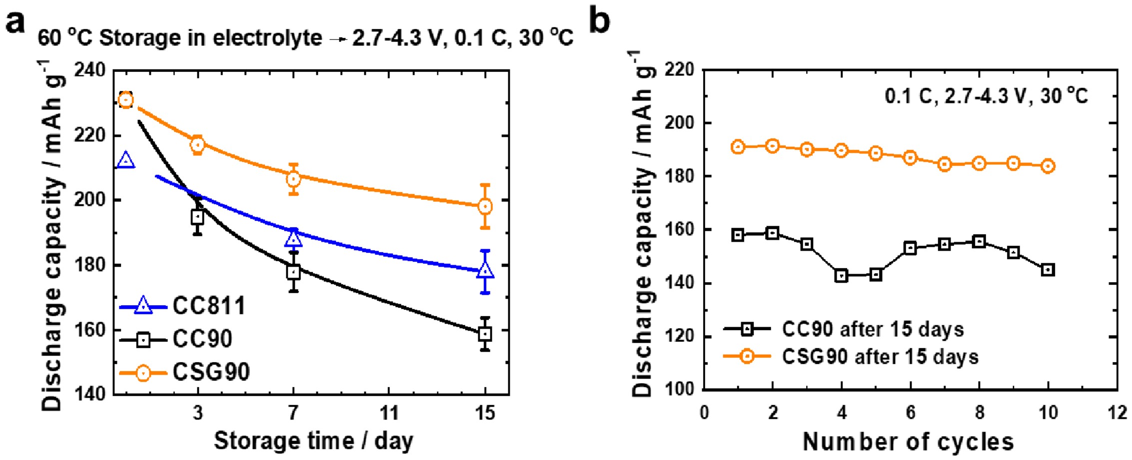

Figure S10. a) Capacity fading trends as a function of storage time after high-temperature storage for 15 days. b) Cycling performance of CC90 and CSG90 after 15 days storage using the 2032 coin-type half cell.

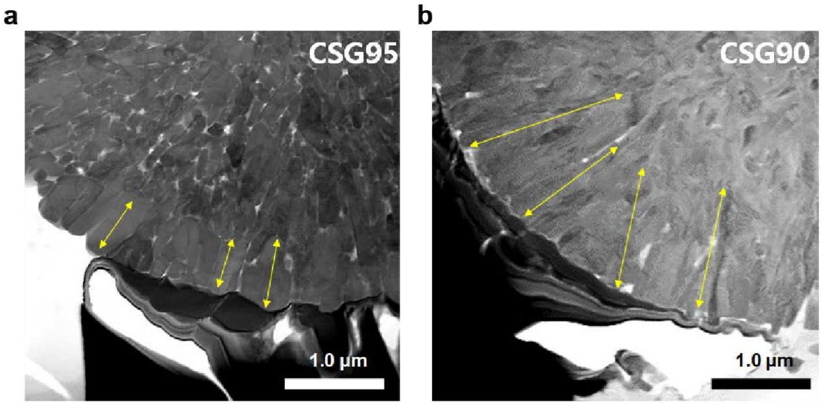

Figure S11. Bright field TEM image; a) CSG95 and b) CSG90.

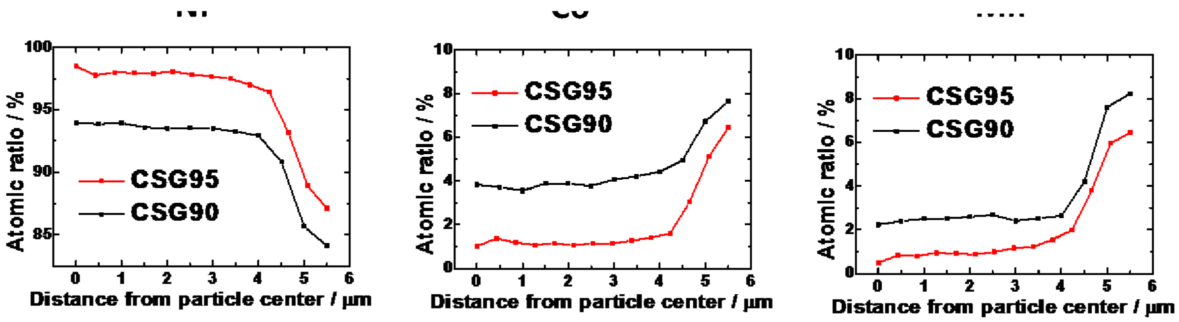

Figure S12. EPMA compositional scan across the CSG95 and the CSG90 lithiated particle.

Table S1. Rietveld refinement on the XRD pattern of CC90 and CSG90.

CC90

Atom	**Wyckoff position**	**x**	**y**	**z**	**Biso**	**Modified Occpancy**
Li 1	3a	0	0	0	[a]1.000	0.982
Ni 1	3b	0	0	0.5	0.336	0.882
Co 1	3b	0	0	0.5	0.336	0.050
Mn 1	3b	0	0	0.5	0.336	0.050
O 1	6c	0	0	0.24092	0.559	2.000
Li 2	3b	0	0	0.5	0.336	0.018
Ni 2	3a	0	0	0	[a]1.000	0.018

CSG90

Atom	**Wyckoff position**	**x**	**y**	**z**	**Biso**	**Modified Occpancy**
Li 1	3a	0	0	0	[a]1.000	0.980
Ni 1	3b	0	0	0.5	0.337	0.880
Co 1	3b	0	0	0.5	0.337	0.050
Mn 1	3b	0	0	0.5	0.337	0.050
O 1	6c	0	0	0.24129	0.566	2.000
Li 2	3b	0	0	0.5	0.337	0.020
Ni 2	3a	0	0	0	[a]1.000	0.020

The modified occupancy for Fullprof = Occ * (general multiplicity / multiplicity) * 12

[a]Fixed value

Sample	**Peak temperature (°C)**	**Enthalpy ($J\ g^{-1}$)**
CC95	184.5	1889
CSG95	191.1	1678
CC90	190.9	1561
CSG90	198.1	1514

Table S2. Results of differential scanning calorimetry for CC95, CSG95, CC90, and CSG90 cathode materials in the delithiated state at 4.3 V.

Table S3. Experimental lattice parameters for lithiated (discharged to 3.68 V) and delithiated (charged to 4.50 V) CSG90 and CC90 particles. Young's modulus values have been measured and reported by Xu et al. for NCM.[1] Poisson's ratio has been measured by Cheng et al.[2]

state	**potential (V)**	***a* (Å)**	***c* (Å)**	***E* (GPa)**	**ν**
shell in CSG90					
discharged	3.68	2.85491	14.22240	-	-
charged	4.50	2.80873	13.73234	111.6	0.25
core in CSG90 and CC90					
discharged	3.68	2.86852	14.17960	-	-
charged	4.50	2.80791	13.61286	111.6	0.25

1. R. Xu, H. Sun, L. S. de Vasconcelos, K. Zhao, *J. Electrochem. Soc.*, **2017**, *164*, A3333.
2. E. J. Cheng, N. J. Taylor, J. Wolfenstinec, J. Sakamoto, *J. Asian Ceramic Soc.,* **2017**, *5,* 113.

References

[1] D. L. Wood III, J. Li, C. Daniel, *J. Power Sources* **2015**, *275*, 234.

[2] J. R. Dahn, U. Von Sacken, C. A. Michal, *Solid State Ionics* **1990**, *44*, 87.

[3] E. Rossen, C. D. W. Jones, J. R. Dahn, *Solid State Ionics* **1992**, *57*, 311.

[4] C. Delmas, I. Saadoune, A. Rougier, *J. Power Sources* **1993**, *43–44*, 595.

[5] T. Ohzuku, A. Ueda, *J. Electrochem. Soc.* **1994**, *141*, 2972.

[6] Z. Liu, A. Yu, J. Y. Lee, *J. Power Sources* **1999**, *81–82*, 416.

[7] M. Yoshio, H. Noguchi, J. Itoh, M. Okada, T. Mouri, *J. Power Sources* **2000**, *90*, 176.

[8] T. Ohzuku, Y. Makimura, *Chem. Lett.* **2001**, *30*, 642.

[9] Y.-K. Sun, S.-T. Myung, H.-S. Shin, Y. C. Bae, C. S. Yoon, *J. Phys. Chem. B* **2006**, *110*, 6810.

[10] H.-J. Noh, S. Youn, C. S. Yoon, Y.-K. Sun, *J. Power Sources* **2013**, *233*, 121.

[11] H.-H. Sun, W. Choi, J. K. Lee, I.-H. Oh, H.-G. Jung, *J. Power Sources* **2015**, *275*, 877.

[12] L. de Biasi, A. O. Kondrakov, H. Geßwein, T. Brezesinski, P. Hartmann, J. Janek, *J. Phys. Chem. C* **2017**, *121*, 26163.

[13] C. S. Yoon, M. H. Choi, B.-B. Lim, E.-J. Lee, Y.-K. Sun, *J. Electrochem. Soc.* **2015**, *162*, A2483.

[14] H.-H. Ryu, K.-J. Park, C. S. Yoon, Y.-K. Sun, *Chem. Mater.* **2018**, *30*, 1155.

[15] C. S. Yoon, H.-H. Ryu, G.-T. Park, J.-H. Kim, K.-H. Kim, Y.-K. Sun, *J. Mater. Chem. A* **2018**, *6*, 4126.

[16] S.-M. Bak, E. Hu, Y. Zhou, X. Yu, S. D. Senanayake, S.-J. Cho, K.-B. Kim, K. Y. Chung, X.-Q. Yang, K.-W. Nam, *ACS Appl. Mater. Interfaces* **2014**, *6*, 22594.

[17] S. Hwang, S. M. Kim, S.-M. Bak, S. Y. Kim, B.-W. Cho, K. Y. Chung, J. Y. Lee, E. A. Stach, W. Chang, *Chem. Mater.* **2015**, *27*, 3927.

[18] C. S. Yoon, D.-W. Jun, S.-T. Myung, Y.-K. Sun, *ACS Energy Lett.* **2017**, *2*, 1150.

[19] A. O. Kondrakov, A. Schmidt, J. Xu, H. Geßwein, R. Mönig, P. Hartmann, H. Sommer, T. Brezesinski, J. JaneK, *J. Phys. Chem. C* **2017**, *121*, 3286.

[20] J.-M. Lim, T. Hwang, D. Kim, M.-S. Park, K. Cho, M. Cho, *Sci. Rep.* **2017**, *7*, 39669.

[21] P. Yan, J. Zheng, J. Liu, B. Wang, X. Cheng, Y. Zhang, X. Sun, C. Wang, J.-G. Zhang, *Nat. Energy* **2018**, *3*, 600.

[22] B. Xiao, X. Sun, *Adv. Energy Mater.* **2018**, *8*, 1802057.

[23] Y.-K. Sun, S.-T. Myung, B.-C. Park, J. Prakash, I. Belharouak, K. Amine, *Nat. Mater.* **2009**, *8*, 320.

[24] B.-B. Lim, S.-J. Yoon, K.-J. Park, C. S. Yoon, S.-J. Kim, J. J. Lee, Y.-K. Sun, *Adv. Funct. Mater.* **2015**, *25*, 4673.

[25] U.-H. Kim, E.-J. Lee, C. S. Yoon, S.-T. Myung, Y.-K. Sun, *Adv. Energy Mater.* **2016**, *6*, 1601417.

[26] J. H. Lee, C. S. Yoon, J.-Y. Hwang, S.-J. Kim, F. Maglia, P. Lamp, S.-T. Myung, Y.-K. Sun, *Energy Environ. Sci.* **2016**, *9*, 2152.

[27] D.-W. Jun, C. S. Yoon, U.-H. Kim, Y.-K. Sun, *Chem. Mater.* **2017**, *29*, 5048.

[28] S. Watanabe, M. Kinoshita, T. Hosokawa, K. Morigaki, K. Nakura, *J. Power Sources* **2014**, *258*, 210.

[29] L. Wu, K.-W. Nam, X. Wang, Y. Zhou, J.-C. Zheng, X.-Q. Yang, Y. Zhu, *Chem. Mater.* **2011**, *23*, 3953.

[30] S. Zheng, R. Huang, Y. Makimura, Y. Ukyo, C. A. J. Fisher, T. Hirayama, Y. Ikuhara, *J. Electrochem. Soc.* **2011**, *158*, A357.

[31] T. Ohzuku, A. Ueda, M. Nagayama, *J. Electrochem. Soc.* **1993**, *140*, 1862.

[32] K.-J. Park, M.-J. Choi, F. Maglia, S.-J. Kim, K.-H. Kim, C. S. Yoon, Y.-K. Sun, *Adv. Energy Mater.* **2018**, *8*, 1703612.

[33] C. S. Yoon, U.-H. Kim, G.-T. Park, S. J. Kim, K.-H. Kim, J. Kim, Y.-K. Sun, *ACS Energy Lett.* **2018**, *3*, 1634.

[34] L. Croguennec, C. Pouillerie, A. N. Mansour, C. Delmas, *J. Mater. Chem.* **2001**, *11*, 131.

[35] Z. Chen, J. R. Dahn, *Electrochim. Acta* **2004**, *49*, 1079.

[36] C. S. Yoon, K.-J. Park, U.-H. Kim, K. H. Kang, H.-H. Ryu, Y.-K. Sun, *Chem. Mater.* **2017**, *29*, 10436.

[37] D. P. Abraham, R. D. Twesten, M. Balasubramanian, I. Petrov, J. McBreen, K. Amine, *Electrochem. commun.* **2002**, *4*, 620.

[38] U.-H. Kim, S.-T. Myung, C. S. Yoon, Y.-K. Sun, *ACS Energy Lett.* **2017**, *2*, 1848.

[39] S. Hwang, W. Chang, S. M. Kim, D. Su, D. H. Kim, J. Y. Lee, K. Y. Chung, E. A. Stach, *Chem. Mater.* **2014**, *26*, 1084.